Parametric study of the gel-combustion synthesis of nanocrystalline ZrO$_2$-based powders

I.O. Fábregas [a,*], D.G. Lamas [a,b,c]

[a] CINSO (Centro de Investigaciones en Sólidos), CITEFA-CONICET, J.B. de La Salle 4397, (B1603ALO) Villa Martelli, Provincia de Buenos Aires, Argentina
[b] Laboratorio de Caracterización de Materiales, Facultad de Ingeniería, Universidad Nacional del Comahue, Buenos Aires 1400, (8300) Neuquén Capital, Pcia. de Neuquén, Argentina
[c] CONICET, Argentina

ABSTRACT

In this paper, we report a study of the effect on the powder morphology of zirconia based solid solutions of several parameters of the synthesis by gel-combustion routes, such as fuel, metal/fuel ratio, composition of the nanopowder, pH of the precursor solution, etc. We evaluated the average crystallite size, BET specific surface area and the degree of agglomeration of the final ceramic nanopowders. The intermediate stages of the synthesis were characterized by Fourier Transform Infrared Spectroscopy, Small Angle X-ray Scattering, X-ray Powder Diffraction, X-ray Absorption Spectroscopy and Infrared Thermography. We found that the precursor gel remained compositionally homogeneous up to the self-combustion step and that in order to obtain a low average crystallite size (<10 nm) and a low degree of agglomeration, the combustion temperature must be tailored to be as high as possible. Finally, a novel gel-combustion route assisted with hydrogen peroxide is reported.

© 2011 Elsevier B.V. All rights reserved.

1. Introduction

Gel-combustion synthesis, and, in general, soft chemical methods, is very popular nowadays as it is a simple and fast synthesis route to produce compositionally homogenous, crystalline, deagglomerated ceramic powders at much lower temperatures than classic ceramic synthesis methods. It allows the facile generation of relatively large quantities of simple [1–6] or complex [7–11] ceramics, which present a nanometric size and/or metastable phases [1,4,9,12–14].

Gel-combustion is based on the formation of an initial gel by thermal concentration of an aqueous mixture of the desired metal nitrates and organic fuels, followed by a combustion process. The reaction between the nitrate ion and the organic fuel is strongly exothermic and the great volume of produced gasses during the combustion promotes the violent disintegration of the precursor gel. A calcination process at moderate temperature eliminates the remaining organic residues. For ZrO$_2$-based powders the synthesis yields a low density powder composed of highly crystalline nanometric grains [12,13] with very small pores between them [15].

Zirconia-based ceramics have been intensely investigated because of their excellent electric and mechanical properties. In particular, TZP ('tetragonal zirconia polycrystals') ceramics exhibit high ionic conductivity at intermediate temperatures and high fracture toughness [16,17]. For example, ZrO$_2$–CeO$_2$ substitutional solid solutions are extensively used as redox or oxygen storage promoters in three-way catalysts [18]

and ZrO$_2$–Y$_2$O$_3$ ceramics are used for several electrochemical devices [19], and biomedical applications [20].

Several authors have studied the influence of certain synthesis parameters on the properties and morphology of the final ceramic powder. Particular attention was paid to the nature and/or mixture of fuels [1,5–9,21] and the role of the oxidizer/fuel ratio [1–3,6,7,9–11,22,23]. Few works reported studies on the influence of the metal/fuel ratio [24,25], the final pH [26,27] or the combustion temperature [1,6,10,28]. As we will demonstrate, this temperature is a very important parameter to tailor properties as the crystallite size or BET surface area. Unfortunately, this temperature was measured on the flame [6,10,28], which may not be representative of the temperature of the solid, or with a thermocouple [1], which may not have reached thermal equilibrium due to the fast propagation of the reaction front. In this paper we report the temperature of the material during combustion.

Additionally, the influence of the mentioned parameters on the final product seems to depend on the material. CeO$_2$[2], (ZrO$_2$)$_{0.92}$(Y$_2$O$_3$)$_{0.08}$ [23], SrCeO$_3$[4] or Gd$_2$O$_3$[6], show a bigger crystallite size as the fuel/oxidizer ratio increases, while the opposite happens for Ce$_{0.8}$Y$_{0.2}$O$_{1.9}$ [22], Ba$_{0.5}$Sr$_{0.5}$Co$_{0.8}$Fe$_{0.2}$O$_3$[7], Y$_2$O$_3$[3] or La$_{0.7}$Ca$_{0.3}$CrO$_3$[11]. Al$_2$O$_3$–tZrO$_2$ [25] composite maintains approximately the same average crystallite size with an increase of the metal/fuel ratio, while for CeO$_2$[24] the average crystallite size diminishes. Nevertheless, all papers report an optimum value depending on the property to be tailored: degree of agglomeration [3,5,22,24], average crystallite size [1–5,7–9,12,13,22,24,25], crystal phase [6,9,10,12,13], average pore size and distribution [5,15], BET specific surface area [2,3,5,22], etc.

* Corresponding author. Tel.: +54 11 47098100x1145; fax: +54 11 47098158.
E-mail address: ifabregas@citefa.gov.ar (I.O. Fábregas).

Currently, nanomaterials have a tremendous technological and basic importance. They present new phenomena and new or enhanced properties as a consequence of their small dimensions [29–40]. In some cases, they are related to quantum effects that arise due to the small number of atoms. For example, CdSe quantum dots have a tunable emission spectrum and higher emission efficiency [39,40]. CeO_2-based nanoceramics present an enhanced ionic conductivity of one order of magnitude higher than their microceramic counterparts [38].

The aim of this work was to optimize the synthesis of ZrO_2-based nanomaterials by gel-combustion. In the particular case of nanoceramics, the advantages are lost if the nano dimensions cannot be retained. Therefore, we have also looked for conditions that increase the sinterability, such as a large BET area.

For this purpose, we studied the influence of the different synthesis parameters (final pH of the gel, fuel type, fuel/metal ratio, final ceramic composition, combustion atmosphere, etc.) on the final ceramic powder. We undertook this study since no article combines all of them in a systematic way for the same material and, in particular, the role of the real combustion temperature, a key factor, is hardly discussed.

2. Experimental

2.1. Gel-combustion synthesis routes

For the non-stoichiometric synthesis routes, 2.25 g of $ZrOCl_2 \cdot 8H_2O$ (Riedel-de Haën, Germany, 99.5%) and $Ce(NO_3)_3 \cdot 6H_2O$ (Alpha Aesar, EE.UU, 99%) or Y_2O_3 (BDH, England, 99.99%), in adequate proportions, were dissolved in water. Then, 50 ml of nitric acid (Merck, Germany, 65%) was added. Since the chloride anions degrade the electrical properties, they were removed by thermal evaporation. This step was carefully controlled to ensure the same content of nitrate in all the samples (see Results and discussion). The fuel (glycine, lysine, alanine or citric acid) was then added and the pH adjusted with ammonium hydroxide (Merck, Germany, 25%). This solution, hereafter named precursor solution, was concentrated by thermal evaporation on a hot plate. Free water was eliminated and a viscous gel appeared. Finally, the gel burned as a consequence of a vigorous exothermic reaction.
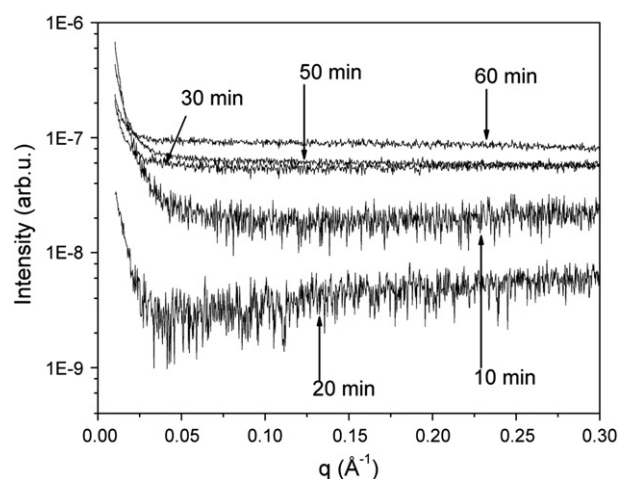
For the stoichiometric synthesis routes, 2.65 g of $ZrO(NO_3)_2 \cdot 6H_2O$ (Fluka, Germany, 99%), and $Y(NO_3)_3 \cdot 6H_2O$ (Sigma, Germany, 99.9%)

Fig. 1. SAXS data of the Z3Y-5 gel (see text for details).

and fuel (lysine or glycine), were dissolved in 25 ml of distilled water according to the following equation:

$$ZrO(NO_3)_2\,3H_2O + bY(NO_3)_3\,6H_2O + cfuel \Rightarrow (ZrO_2\,b2Y_2O_3) + eCO_2 + fH_2O + gN_2$$
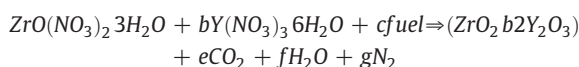
where coefficients c, e, f and g depend on the desired ceramic composition and fuel.

This precursor solution was concentrated by thermal evaporation on a hot plate. As for the non-stoichiometric routes, a viscous gel appeared after the evaporation of free water and, albeit less violent, a combustion reaction took place.

Table 1 reports the different synthesis routes studied for the synthesis of ZrO_2–Y_2O_3 or ZrO_2–CeO_2 powders, while Diagram 1 displays schematically the different synthesis steps.

Typically, for both routes, the combustion starts in one spot and quickly propagates. None of the syntheses showed precipitation or turbidity.

Additionally, a Z3Y-5 powder was synthesized in a graphite cell. This cell maintained a temperature gradient that kept the gel melted at the hot end and solidified at the cold one (see Diagram 2). In order to ensure an even distribution in the cell, the gel was poured in its liquid state.

Hereafter the citric acid containing gels will be referred as CIT while the amino acids ones as AA. The as-synthesized materials (previous to the calcination step) will be referred as ashes.

Table 1

Stoichiometric and non-stoichiometric synthesis routes studied for the generation of ZrO_2–Y_2O_3 or ZrO_2–CeO_2 nanocrystalline ceramic powders. Ala: alanine. Lys: lysine. Gly: glycine. Cit: citric acid. SO: purged in N_2. Stoi: stoichiometric route, the other gels were obtained by the non-stoichiometric route.
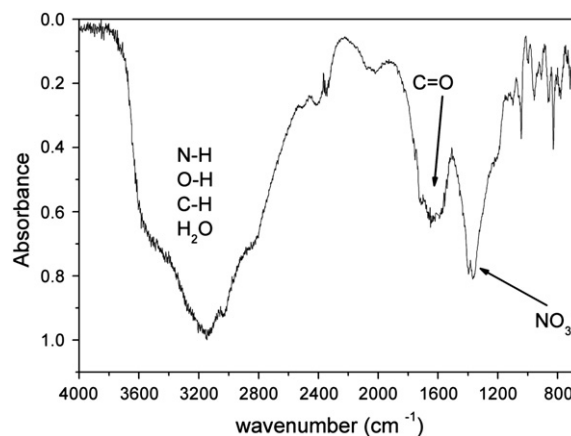
Oxide composition	Fuel	Fuel/metal ratio	Final pH/type	Code
ZrO_2–2.8 mol% Y_2O_3	Lys	1.32	5	Z3Y-Lys
ZrO_2–2.8 mol% Y_2O_3	Lys	0.30	Stoi	Z3Y-Lys-Stoi
ZrO_2–2.8 mol% Y_2O_3	Ala	3	5	Z3Y-Ala
ZrO_2–2.8 mol% Y_2O_3	Cit	1.25	5	Z3Y-1.25Cit
ZrO_2–2.8 mol% Y_2O_3	Cit	2.5	5	Z3Y-5
ZrO_2–2.8 mol% Y_2O_3	Cit	2.5	5	Z3Y-5-SO
ZrO_2–2.8 mol% Y_2O_3	Cit	3.75	5	Z3Y-3.75Cit
ZrO_2–2.8 mol% Y_2O_3	Cit	2.5	2	Z3Y-2
ZrO_2–2.8 mol% Y_2O_3	Cit	2.5	2.5	Z3Y-2.5
ZrO_2–2.8 mol% Y_2O_3	Cit	2.5	4	Z3Y-4
ZrO_2–2.8 mol% Y_2O_3	Cit	2.5	6	Z3Y-6
ZrO_2–2.8 mol% Y_2O_3	Cit	5	5	Z3Y-H_2O_2[a]
ZrO_2–2.8 mol% Y_2O_3	Gly	1.14	Stoi	Z3Y-Gly-Stoi
ZrO_2–2.8 mol% Y_2O_3	Gly	5	5	Z3Y-Gly
ZrO_2–5 mol% Y_2O_3	Cit	2.5	0	Z5Y
ZrO_2–10 mol% Y_2O_3	Cit	2.5	5	Z10Y
ZrO_2–12 mol% Y_2O_3	Cit	2.5	5	Z12Y
ZrO_2–15 mol% Y_2O_3f	Gly	5	5	Z15Ce

[a] 10 ml of 200vol H_2O_2 were added before neutralization.

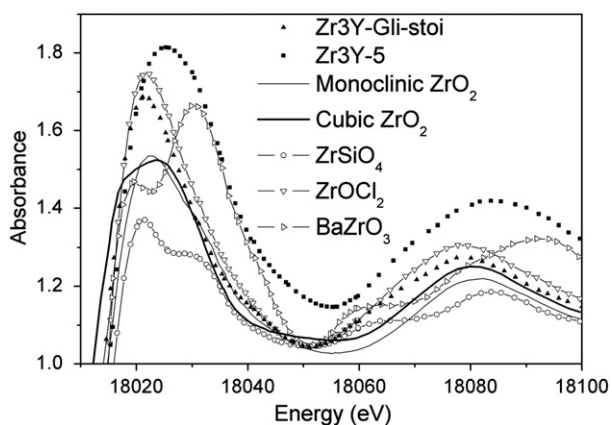Fig. 2. FTIR spectra of the Z3Y-5 gel.

Fig. 3. XANES spectra at the Zr K-edge of the structural standards and selected samples.

2.2. Characterization

Due to the swiftness of the combustion reaction, a variable quantity of organic residues, composed mostly of carbon and oxidized organic matter [3,4,22], remained on the ashes. To remove the organic residue, a calcination step at 630 °C for 2 h was necessary. This organic residual content was determined gravimetrically, carefully weighting the samples before and after calcination.

The combustion temperature was measured with a Jenoptik Varioscan 3022 infrared camera. This camera acquires data in two dimensions once every second, covering the whole combustion zone simultaneously. The temperatures reported in Table 6 are the highest measured for each synthesis.

Fourier transformed infrared spectroscopy (FTIR) was performed both on the gels and combustion gasses with a Nicolet 520P FTIR spectrometer (2 cm^{-1} resolution). All the gels were measured in diffuse reflectance mode, supported on a stainless steel sampleholder. A KBr windowed cell was used to measure the combustion gasses. 128 spectra were acquired for all samples.

Small-angle X-ray scattering (SAXS) data of melted samples were taken, in transmission mode, at the D11A-SAXS1 beamline of the Brazilian Synchrotron Light Laboratory (LNLS, Campinas, Brazil). A Si (111) monochromator, asymmetrically cut and horizontally bended, provided horizontally focused X-rays at a wavelength of 1.608 Å. SAXS intensity was registered along the vertical direction, using a one-dimensional position-sensitive gas detector, as a function of the scattered vector module q.

X-ray absorption spectroscopy (XAS) spectra of the gels were acquired in the D04B-XAFS1 beamline [41] of the LNLS, in transmission mode. A Si (220) monochromator for Zr and Y K-edges was used. The energy was calibrated with a Zr metallic foil. The spectra were taken at room temperature. Both the near (XANES) and extended regions (EXAFS) above the absorption edge were measured. Table 2 reports the structural standards used for XANES analysis to determine the environment around Zr and Y in the gels. Three spectra were taken for each gel and its average used to perform the analysis. To optimize the signal/noise ratio, the thickness of the pellets used for data acquisition was adjusted to obtain a total absorbance above the edge of 1.5.

Data reduction for the EXAFS region of the spectra was performed with the EXAFS 2001 code [42]. A linear fit to the pre-edge data was subtracted to make the background correction and a fifth grade polynomial was fitted to the post-edge data. The inelastic contribution (S_0^2) for the Zr and Y K-edges was calculated using a BaZrO$_3$ standard, obtaining a value of 0.9. The FEFFIT code [43] was used in the quantitative fitting of the k^3-weighted EXAFS signal, utilizing theoretical amplitudes and phases calculated by the FEFF8 code [44]. A window between 3 and 12 Å^{-1} was selected for both Zr and Y in K-space, while windows between 1 and 4 Å, for Zr, and 1–2.5 Å, for Y, were selected in R-space. Since oxygen, nitrogen and carbon have similar scattering sections and are thus indistinguishable backscatterers in EXAFS analysis, their dispersion paths were modeled using only Zr–O paths. The first and second spheres of the AA gels were modeled with 3 oxygen subshells and one Zr shell, respectively. For the CIT gels, the first sphere was modeled with one oxygen shell while the second sphere was modeled with one Zr shell and one oxygen shell. The local environment around Y was modeled with a single oxygen sphere.

X-ray powder diffraction (XPD) data were taken, for both ashes and ceramic powders, with a Philips PW 3710 laboratory diffractometer, equipped with a graphite monochromator, operated at 40 kV and 30 mA and using Cu–Kα radiation. Data were taken in the 2θ = 20–90° range and particular attention was given to the 2θ = 27–33° range to test for the presence of monoclinic phase and to determine the crystallite size, D. The latter was calculated from the full-width at half-maximum (FWHM) of the 111 Bragg peak of the tetragonal or cubic phases by

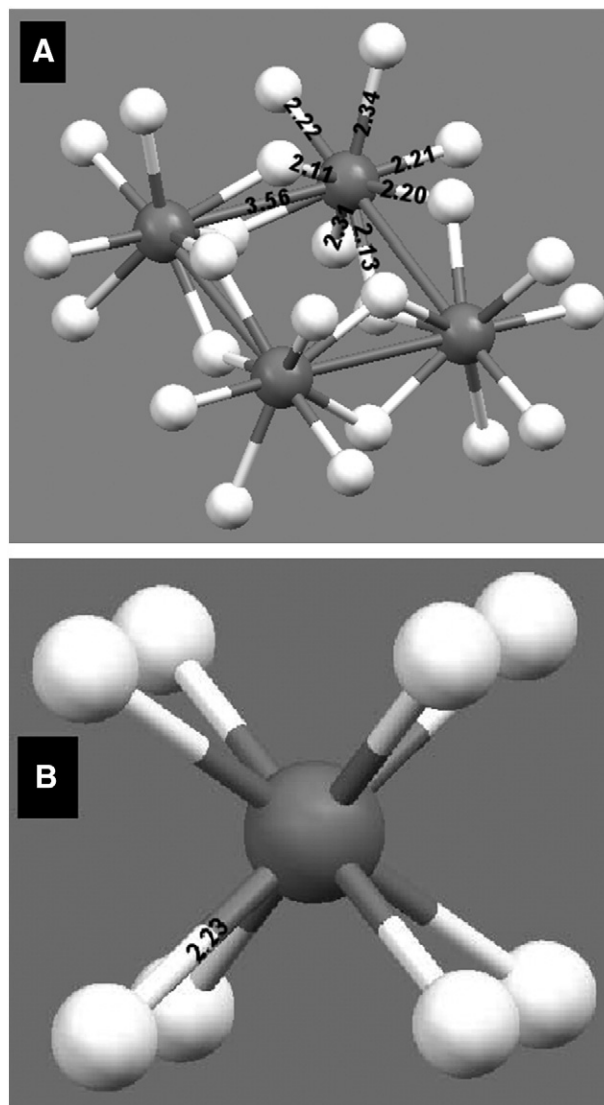**Fig. 4.** A) Local environment around Zr for ZrOCl$_2$·8H$_2$O (zirconyl chloride). B) Local environment around Zr for cubic ZrO$_2$. The numbers over the bonds in the figure are the bond length in Å. Dark gray (Zr atoms), white (O atoms).

means of the Scherrer equation [45]. The FWHM was corrected by the instrumental broadening, measured with a LaB$_6$ standard (NIST SRM 660).

BET specific surface area, S$_{BET}$, was measured with nitrogen adsorption at 77 K with an Autosorb-1 equipment. Prior to the measurements all the samples were degassed at 250 °C for 2 h under 0.02 Pa. The value of S$_{BET}$ allows the calculation of two important parameters: the average particle size and the degree of agglomeration. The first is an average diameter of the particles determined from S$_{BET}$ under the assumption of a monodisperse distribution of dense spherical particles, calculated according to:

$$d = 6 / (S_{BET} * \rho)$$

where d is the average particle size, S$_{BET}$ is the BET specific surface area and ρ is the density (6 g/cm^3 in the case of ZrO$_2$–Y$_2$O$_3$). The degree of agglomeration is the ratio between d and the experimental average crystallite size, and gives an estimate of the agglomeration of the sample.

Scanning electron micrographs of the ceramic powders, after gold sputtering, were taken in a FESEM DSM 982 Gemini at 3 keV.

3. Results and discussion

3.1. Precursor gels

Fig. 1 displays different SAXS patterns for the Z3Y-5 synthesis as a function of the remaining time to the moment of combustion. A quick fall at low q and a subsequently uniform value in the rest of the studied q range is observed. Similar patterns were obtained for all the other routes. The shape of these curves indicates, according to X-ray scattering theory, that the gel was homogeneous up to the moment of the combustion reaction. This is an important fact, because the presence of inhomogeneities in the precursor gel would cause compositional inhomogeneities in the ceramic powder and degrade their electrical and/or mechanical properties.

Fig. 2 displays the Z3Y-5 gel FTIR spectrum. In general, the spectra for all the other gels were similar but for some minor details. The wide band between 2600 and 3700 cm^{-1} is assigned to the vibrations of the O–H (water and acids), C–H and N–H (amines) bonds [46]. The shoulder at 2400 cm^{-1} is assigned to a nitrate vibration [46]. The bands at approximately 1700 and 1350 cm^{-1} are assigned to the vibration of the carboxyl C=O double bond and to a wide nitrate band, respectively [46]. The weak band at approximately 2050 cm^{-1} is assigned to the cyanide C≡N triple bond vibration [47].

To establish the speciation of the carboxyl groups on the different gels, the bands centered around 1600 cm^{-1}, assigned to the O–C–O asymmetric vibration (carboxylate state), and 1720 cm^{-1}, assigned to the C=O stretching vibration (carboxylic state), [46] were used. Citric acid is a tricarboxylic acid with pKa values of 3.13, 4.76 and 6.4 [48], while the amino acids used in this study have pKas lower than 2.5 [48]. Therefore the presence of carboxylate is expected on all the samples due to the deprotonation effect of the pH (see Fig. S1). The exception was the Z5Y-0 gel, where there was carboxylate present, as evidenced by the 1600 cm^{-1} band shown in Fig. S1. This presence cannot be explained from deprotonation, since at pH = 0 all the carboxyl groups should be completely protonated. In this case the presence of the carboxylate can only be explained if the carboxyl groups formed a complex with the cations. It is also known that at the final pH of the precursor solutions the cations are insoluble [49,50], so that complexation must be occurring in all the gels. EXAFS results support, in an independent manner, this conclusion (see Section 3.1.1). The fuel's complexing capacity thus ensured the homogeneity of the gel and therefore of the final ceramic.

To establish the speciation of the nitrate, the bands centered at approximately 1025 cm^{-1} (bidentate complexed nitrate) or 1045 cm^{-1} (free nitrate) [51] were used. The CIT samples only presented free
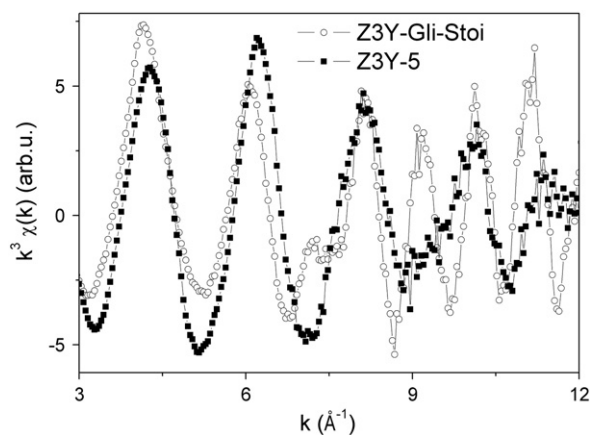
Fig. 5. EXAFS signal at the Zr K-edge for the Z3Y-5 and Z3Y-Gly-stoi gels.

nitrate (see Fig. S2), while the AA samples showed both free (see Fig. S2) and complexed nitrate (also found in [51] in sols of pure zirconia). The most likely explanation for the absence of complexed nitrate in the CIT gels is the steric impediment of the bulky citric acid. As the oxygens of the carboxylic groups complexed the cations, the carbon skeleton prevented the access of other molecules, like nitrate, water, cyanide, etc., (see Section 3.1.1 for a more detailed discussion).

The speciation of the cyanide was also determined. A band at approx. 2020 cm^{-1}, assigned to monodentate cyanide complexes [51,52], appeared in the AA gels, but it was not possible to determine its presence in the CIT gels, because here there were overlapping bands between nitrate and cyanide, so any observations were inconclusive (Fig. S3). Therefore, the AA gels had complexed cyanide, while nothing could be concluded for the CIT gels. Probably, as was the case for the nitrates, the citric acid blocked the access of the cyanide and it was free in these gels.

The speciation of the amino groups could not be established due to overlapping bands and high absorbance from high fuel concentrations.

3.1.1. Local atomic order

Fig. 3 displays XANES spectra for the studied structural standards and also the spectrum of Z3Y-Gli-stoi and Z3Y-5. All the AA gels showed very similar spectra to that of zirconyl chloride. Contrarily,
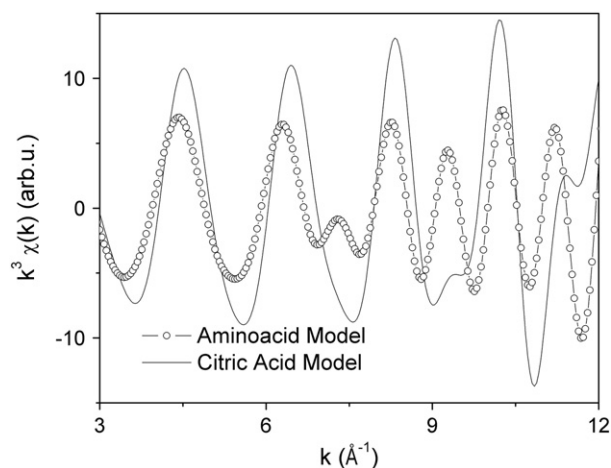
Fig. 6. Theoretic EXAFS signals for different local order models around Zr.

the CIT gels spectra did not look like any single one structural standard, but a mixture between zirconyl chloride and cubic zirconia (see Fig. 4A and B and Table 2 for their local environment around Zr). The studied gels could be thus separated in two distinctive groups, each with a different environment around Zr. Initially, the same model for the AA gels was used for the CIT gels, but this procedure failed to reproduce all the features of the EXAFS signal. Since the CIT gel XANES spectra also presented characteristics of a cubic environment, the EXAFS signal was alternatively modeled with only one oxygen sphere. For the second shell it was also necessary to add "oxygens" at a similar distance to that of the Zr–Zr bond. This procedure achieved a better agreement between the modeled and experimental signals (compare Figs. 5 and 6), and was subsequently used.

It is known that Zr as free aqueous Zr^{4+} is virtually non-existent and even on strongly acidic solutions (1–2 M HCl) Zr is found in a polymerized form [54]. Also, in both zirconyl nitrate and chloride (the reagents used in these syntheses) Zr atoms are found as the tetramer $[Zr_4(OH)_8(H_2O)_{16}]^{8+}$ form (Fig. 4A); a form that was also found in studies of Zr in solution (using XPD, SAXS, light scattering and low temperature EXAFS [53–56]). Considering that the pH in most of the gels was above 4, the similarity of the Zr–O and Zr–Zr bond distances and coordination numbers between those of the tetramer and the results reported in Tables 3 and 4 for the AA and CIT gels it is possible to conclude that the Zr was in the tetramer form in both the AA and the CIT gels. It is important to mention that the coordination numbers determined by EXAFS analysis have large relative errors, so deviations from the tetramer coordination are not significant.

The most likely origin for the additional "oxygens" needed to model the CIT gel EXAFS spectra are carbon atoms from the citric acid. If we assume that Zr was complexed by the oxygens of the citric acid carboxyl groups, some of the skeleton carbon atoms are located at a distance of approximately 3.5 Å from the Zr atom, whereas the Zr–Zr bond length is 3.52 Å. This supports the assumption made in the FTIR section that the fuels complexed the cations.

XAS analysis at the Zr K-edge demonstrated that the samples could be classified into two distinctive groups, the AA and the CIT gels. For this reason, one gel from each group was selected to carry out the EXAFS analysis at the Y K-edge, Z3Y-Gly-Esteq and Z3Y-4, respectively. The XANES spectra at the Y K-edge of these two precursor gels were similar to each other and to the CIT gels at the Zr K-edge. Then, the local environment around Y was modeled as the CIT gels.

Fig. 7 displays the K-weighted EXAFS signal for the Z3Y-4 gel. The loss of signal for k greater than 9 Å^{-1} is evident. This indicated that there was not a second sphere around Y and, therefore, it was isolated in the gel. All of the other samples presented a similar signal. Table 5 reports the results obtained from the EXAFS analysis at the Y K-edge.
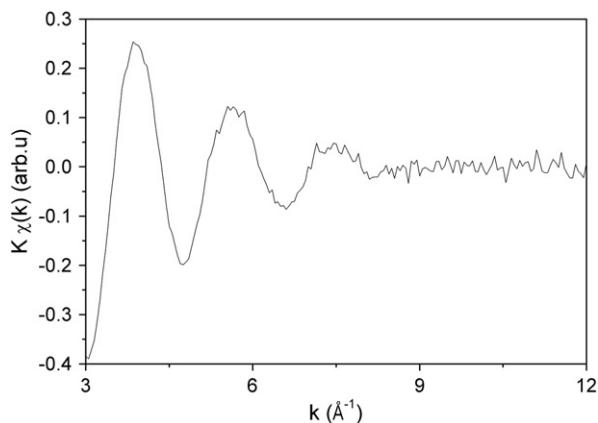
The chelating atoms around Y and Zr could be oxygen, nitrogen or carbon which could belong to water, nitrate, the carboxyl groups, the amine groups and/or cyanide. As discussed above (see Section 3.1) both the citric acid and the amino acids complexed the cations but, simultaneously, the citric acid blocked the access to them to any other molecule, and the presence of coordinated water and/or amine groups could not be discarded in the AA gels. The gels containing L-lysine, in spite of being a bulky molecule, had no sufficient fuel (fuel/metal ratio of 0.30) to block access to the Zr atom. Glycine and L-alanine are small amino acids that do not present a big steric impediment, so the access to the cations was not obstructed for the AA gels.

The data summarized in Tables 3, 4 and 5 shows that the cation–$O_{chelant}$ bond lengths are slightly longer for the AA gels than for the CIT gels. This fact indicates that the citric acid complex is stronger than the amino acid ones. A fact supported by the complex formation constants. The constant for citric acid (~10^{10}, [57]) is greater than for amino acids (~10^5, [58]). A bigger formation constant means a stronger bond and a shorter bond distance.

3.2. Combustion and ashes

Diagram 2 displays the temperature gradient of the graphite cell for a Z3Y-5 synthesis. The gel was in its solid state from 42 °C up to around 160 °C. The combustion started at the hottest spot and then self-propagated through the melted gel. Several simultaneous events contribute to explain this fact: the exothermic ($\Delta H_r^o = -37$ kJ/mol [59]) decomposition of NH_4NO_3 to H_2O and N_2O (an oxidizing gas), the endothermic ($\Delta H_r^o = 176$ kJ/mol [59]) dissociation of NH_4NO_3 to NH_3 and HNO_3, the exothermic oxidation of citric acid, the exothermic oxide formation (see below), and, lastly, the heat removal caused by the escaping hot gasses. In this situation a thermal equilibrium is established that explains why the combustion only occurred in the melted gel, as reported by several authors [60–64], but did not self-propagate into the solid region (where additional heat would be necessary to melt the gel). Besides, the exothermic decomposition of NH_4NO_3 only occurs in the liquid state above 200 °C [59].

Fig. 8 shows the FTIR spectrum of Z3Y-5 as a typical example of the gasses generated in the combustion process. Selected samples are shown in Fig. S4. All samples presented a similar spectra but for Z15Ce and Z3Y-5 SO. N_2O, NO, NO_2, CO and CO_2 (principal absorption bands located around 2220 cm^{-1}, 1870 cm^{-1}, 1610 cm^{-1}, 2130 cm^{-1} and 2340 cm^{-1}, respectively [46]) were produced by all the samples. These gasses came from the thermal decomposition of NH_4NO_3[54,59,65] or the combustion of organic matter [60]. HCN (principal band at 710 cm^{-1}[46]), a molecule that is easily generated in an oxidizing

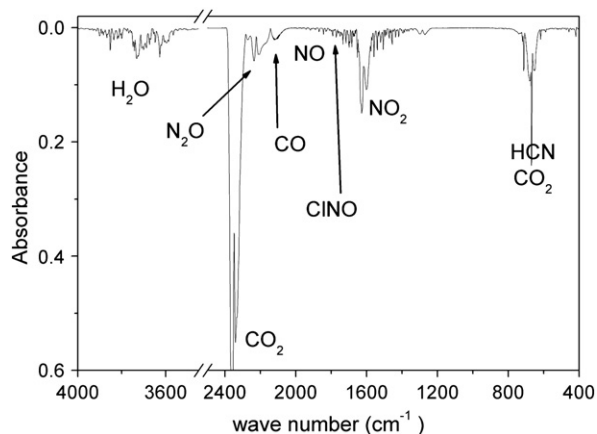Fig. 7. EXAFS signal at the Y K-edge for the Z10Y gel.

Fig. 8. FTIR spectra of the combustion gasses (for clarity, not all the spectra are shown).

environment in the presence of nitrogen [66–68], was also produced. These gasses, plus water vapor, justify all of the observed peaks in the FTIR spectra.
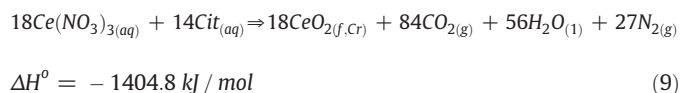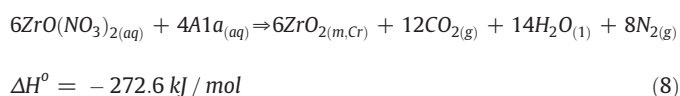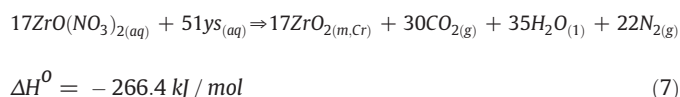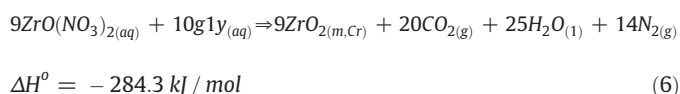
The Z15Ce combustion generated a high proportion of CO_2, which is consistent with the fact that ZrO_2 doped CeO_2 ceramic powders are very good catalysts for the total oxidation of organic matter [69]. The difference on the Z3Y-5 SO spectrum is because it was performed in an oxygen-free environment, generating higher quantities of reduced nitrogen oxides and CO. This synthesis was performed in order to confirm that atmospheric oxygen is not essential for the synthesis. In fact, we observed that all the combustion reactions always started when the temperature was above 210 °C, a temperature at which NH_4NO_3 decomposes (see Section 3.1), so the onset of the combustion could be related to the generation of N_2O. Finally, in some of the non-stoichiometric routes, traces of NOCl (principal band around 1800 cm^{-1}) were detected (see Fig. 8). The NOCl is most likely generated according to the following reaction:

$$3Cl^-_{(aq)} + 4HNO_{3(aq)} \Rightarrow 3NO^-_{3(aq)} + Cl_{2(g)} + NOCl_{(g)} + 2H_2O_{(1)}.$$
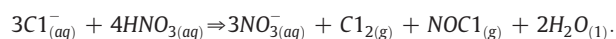
The detection of NOCl confirmed a previously proposed hypothesis by our group for the removal of the chlorides [70]. N_2 is a homonuclear diatomic molecule, so while it was surely generated, it is not possible to be detected by FTIR.

Table 6 summarizes the measured combustion temperatures, the content of organic residues in the ashes, the mass/mass percentage of the oxide in the gels (% oxide) and the ashes' average crystallite size (D_{ash}). It is evident that the combustion temperature did not depend on the final pH, for a pH higher than 2, or on the route 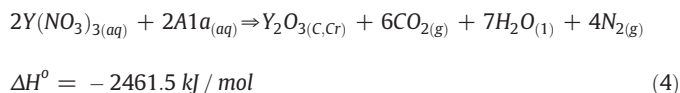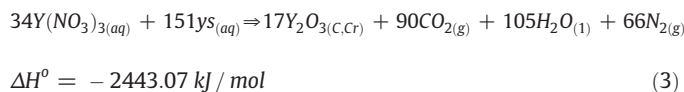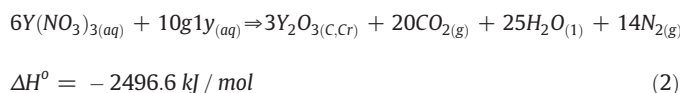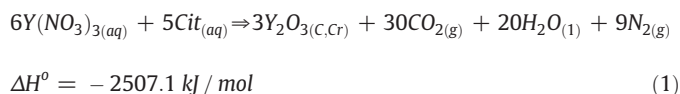used. It essentially depended on the fuel type. These observations suggest that, for a pH≥4, the combustion temperature was independent of the ammonium content. In order to understand its dependence as a function of ceramic composition or fuel used, the molar enthalpy of formation (ΔH^o_f) of the ceramic powders was calculated. Since the ammonium content or route did not influence the combustion temperature, the stoichiometric reaction between the metal nitrates (Zr, Y or Ce) and the fuels (alanine, glycine, lysine or citric acid) was

considered to calculate the enthalpies of formation of the pure oxides from the reactants in their aqueous state.

$$6Y(NO_3)_{3(aq)} + 5Cit_{(aq)} \Rightarrow 3Y_2O_{3(C,Cr)} + 30CO_{2(g)} + 20H_2O_{(1)} + 9N_{2(g)}$$

$$\Delta H^o = -2507.1 \ kJ/mol \tag{1}$$

$$6Y(NO_3)_{3(aq)} + 10gly_{(aq)} \Rightarrow 3Y_2O_{3(C,Cr)} + 20CO_{2(g)} + 25H_2O_{(1)} + 14N_{2(g)}$$

$$\Delta H^o = -2496.6 \ kJ/mol \tag{2}$$

$$34Y(NO_3)_{3(aq)} + 151ys_{(aq)} \Rightarrow 17Y_2O_{3(C,Cr)} + 90CO_{2(g)} + 105H_2O_{(1)} + 66N_{2(g)}$$

$$\Delta H^o = -2443.07 \ kJ/mol \tag{3}$$

$$2Y(NO_3)_{3(aq)} + 2Ala_{(aq)} \Rightarrow Y_2O_{3(C,Cr)} + 6CO_{2(g)} + 7H_2O_{(1)} + 4N_{2(g)}$$

$$\Delta H^o = -2461.5 \ kJ/mol \tag{4}$$

$$9ZrO(NO_3)_{2(aq)} + 5Cit_{(aq)} \Rightarrow 9ZrO_{2(m,Cr)} + 30CO_{2(g)} + 20H_2O_{(1)} + 9N_{2(g)}$$

$$\Delta H^o = -287.7 \ kJ/mol \tag{5}$$

$$9ZrO(NO_3)_{2(aq)} + 10gly_{(aq)} \Rightarrow 9ZrO_{2(m,Cr)} + 20CO_{2(g)} + 25H_2O_{(1)} + 14N_{2(g)}$$

$$\Delta H^o = -284.3 \ kJ/mol \tag{6}$$

$$17ZrO(NO_3)_{2(aq)} + 51ys_{(aq)} \Rightarrow 17ZrO_{2(m,Cr)} + 30CO_{2(g)} + 35H_2O_{(1)} + 22N_{2(g)}$$

$$\Delta H^O = -266.4 \ kJ/mol \tag{7}$$

$$6ZrO(NO_3)_{2(aq)} + 4Ala_{(aq)} \Rightarrow 6ZrO_{2(m,Cr)} + 12CO_{2(g)} + 14H_2O_{(1)} + 8N_{2(g)}$$

$$\Delta H^o = -272.6 \ kJ/mol \tag{8}$$

$$18Ce(NO_3)_{3(aq)} + 14Cit_{(aq)} \Rightarrow 18CeO_{2(f,Cr)} + 84CO_{2(g)} + 56H_2O_{(1)} + 27N_{2(g)}$$

$$\Delta H^o = -1404.8 \ kJ/mol \tag{9}$$

where m is the monoclinic phase, f is the fluorite or pseudofluorite phase, C is the cubic phase and Cr means a crystalline phase.

The relevant thermodynamic data to calculate the formation enthalpies 1 to 9 were taken from Refs. [48,71–78] and are reported in Table S1. With these enthalpies and additional data (also reported in Table S1) it was possible to calculate the heat released in the formation of the ZrO_2 based solid solutions.

These calculations helped explain the increase in combustion temperature with increasing Y_2O_3 or CeO_2 content and, qualitatively, the relative combustion temperatures when using different fuels. Increasing the Y_2O_3 content releases more heat and the temperature reached on combustion should be higher, which is exactly what happens when we considered the combustion temperatures of the Z3Y-5, Z10Y and Z12Y samples. These samples have an increasing standard enthalpy of formation of −331.8, −502.5, and −548.6 kJ/mol, respectively, with increasing combustion temperatures of 645, 739 and 776 °C, respectively. The Z15Ce sample has a ΔH^o_f of −438.6 kJ/mol and its predicted combustion temperature should be between those of the Z3Y-5 and Z10Y samples. Actually, it was higher than any of the others (1009 °C). This is related to the fact that the specific heat capacity for Z15Ce is lower than those of Z3Y or Z10Y oxides ([79–81] and especially [82–84], that report high temperature data). So, even if Z15C has a lower ΔH^o_f, a higher combustion temperature was reached.

It is more difficult to explain the dependency of the combustion temperature on the type of fuel. The enthalpies of formation predict that Z3Y-Lys ($\Delta H^o_f = -309.2$ kJ/mol) should have the lowest combustion

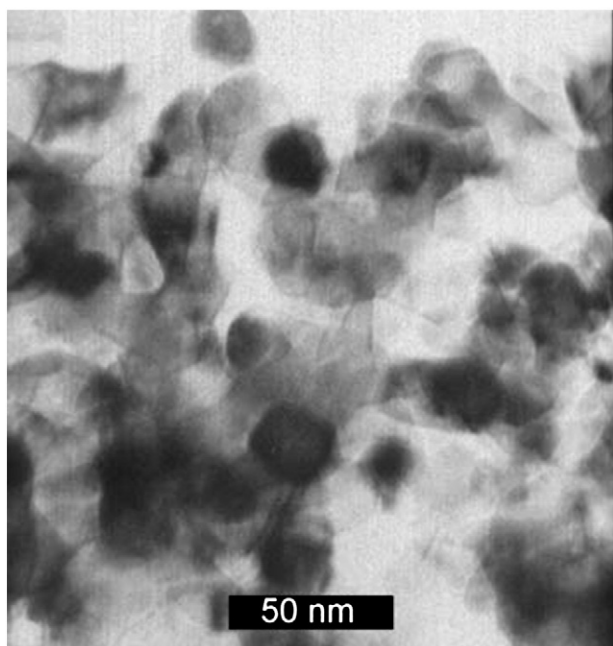**Fig. 9.** TEM micrograph for Z3Y-1.25Cit.

temperature, followed by Z3Y-Ala ($\Delta H_f^o = -315.7$ kJ/mol), then Z3Y-Gly ($\Delta H_f^o = -328.1$ kJ/mol) and finally Z3Y-5 ($\Delta H_f^o = -331.8$ kJ/mol). The measured combustion temperatures presented this general trend, the lowest combustion temperature was that of Z3Y-Lys (440 °C), followed by Z3Y-Ala (518 °C), but Z3Y-5 (645 °C) and Z3Y-Gly (664 °C) were inverted. Z3Y-Gly had a slightly lower ΔH_f^o than Z3Y-5, and therefore should have a lower combustion temperature than Z3Y-5. The fact that the volume of gasses released is greater on the combustion of citric acid than of glycine, therefore removing more heat, might explain this discrepancy. Nevertheless, it will be the object of a further study.

If the combustion temperatures of the Z3Y-1.25Cit (540 °C), Z3Y-5 (645 °C) and Z3Y-3.75Cit (600 °C) samples are considered, a dependency on the metal/fuel ratio (and simultaneously on the fuel/nitrate ratio, see the Experimental section) is evident. According to propellant chemistry, the ratio of the net oxidizing valence to the net reducing valence (Φ) of a mixture, determines its heat of reaction on combustion [85]. The theory considers quantitatively and qualitatively the atomic composition of the mixture irrespective of in which molecule the atoms are present. When Φ equals 1, the maximum amount of energy is released on combustion. While Φ cannot be precisely established for these samples, this observation explains why the combustion temperature depends on the nitrate/metal ratio. It might also explain why the Z3Y-5 sample, which probably had Φ closest to 1, had the highest combustion temperature of the series.

A decrease in combustion temperature occurred both for Z3Y-2 and Z5Y, with a final pH of 2 and 0, respectively. For Z3Y, it coincides with a change in the crystalline phase of the ceramic powder. For Z5Y, the decrease in the combustion temperature is less evident, but its dependency on the Y_2O_3 content predicts a combustion temperature of around 700 °C (for a pH ≥ 4), whereas it was actually 610 °C. This dependency on the pH is not well understood yet.

Noteworthy, both synthesis routes generated ashes that were already well crystallized, except for Z3Y-Lys, which was amorphous. The volume and/or speed of the expelled gasses and the combustion temperature did not seem to influence the crystallite size of the ashes (D_{ash}, reported in Table 6), but, interestingly, we found a relationship between the mass/mass percentage of the oxide in the gel (referred hereafter as oxide content) and D_{ash}. Whenever the oxide content diminished, D_{ash} was smaller. This can be explained by a dilution effect analog to that described by the classical theory of nucleation and precipitation [54]. The more diluted the cations are, less cations can diffuse toward a nucleation center, thus generating smaller crystallites.

Finally, no clear relationship between the content of organic residues in the ashes and the combustion temperature could be established for the Z3Y series. The low content of residues found for the Z15Ce sample is related to the high temperature reached during the process of combustion and/or the fact that ZrO_2–CeO_2 is an excellent catalyst for the oxidation of organic matter [69]. The low content of residues in the samples synthesized by stoichiometric routes compared with non-stoichiometric routes is probably because the respective precursor gels contained less fuel (see Table 6). The nitrate/fuel ratio could also have an influence, but it was not possible to calculate it for the non-stoichiometric routes, so further discussion would be pointless.

3.3. Ceramic powders

Table 6 also summarizes the average crystallite size (D_{powder}), the BET specific surface area (S_{BET}), the average particle size (d) and the degree of agglomeration (d/D_{powder}) of the synthesized ceramic powders. All of them were single-phased and presented the tetragonal or cubic phases, according to their composition. The exception was the Z3Y-2 sample that presented the stable monoclinic phase.

A TEM micrograph (Fig. 9) for Z3Y-1.25Cit shows agglomerates of about 70 nm, a little bigger than the d/D_{powder} calculated from BET but in good accordance with it. A similar result was obtained for the other samples.
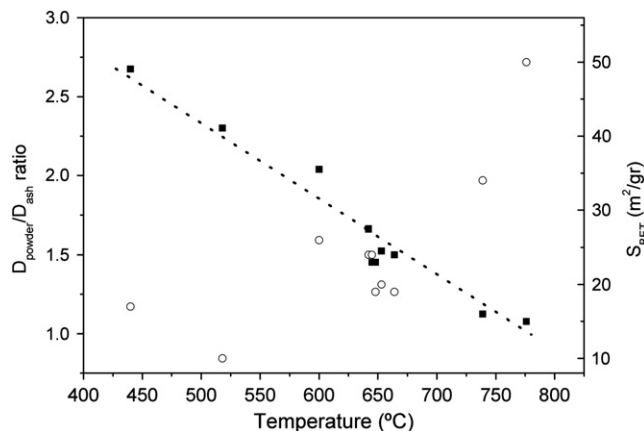

Fig. 10. Ratio between the average crystallite size after and before calcinations and SBET as a function of combustion temperature. (▪) Ratio, (○) S_{BET}.

As the aim of this work was to generate nanocrystalline powders, particular attention was given to those parameters that could diminish crystallite size. From Table 6 we see that as a general trend, the D_{powder}/D_{ash} ratio tended to one (Fig. 10) and that D_{powder} decreases with increasing combustion temperature. At higher combustion temperatures, the crystallites were consolidated better and, therefore, they did not grow so much in the calcination step, particularly when this step was carried out at lower temperatures than that reached during the combustion reaction. Then, the combustion temperature is a critical factor to retain a small average crystallite size. The exception was ZrO_2–15 mol% CeO_2, which presented a bigger crystallite size in spite of its high combustion temperature (1009 °C), probably due to the fact that CeO_2-based materials are more reactive. As an example, compare the average crystallite size of CeO_2–Y_2O_3 (approx. 20 nm) [86] against ZrO_2–Y_2O_3 (approx. 8 nm) [87] for powders treated at 500 °C in both cases. Another effect to consider is that additional crystallite growth may be induced by the leftover organic residues. They can produce a high local temperature when burned in the calcination step. Fortunately, the content of organic residues had no effect on D_{powder}. If we observe, for example, the combustion temperature, the content of organic residues and D_{powder} of the Z3Y-4/5/6 samples, it can be noted that they presented the same combustion temperature and essentially the same D_{powder}, but different contents of residues.

Another aim of this work was to obtain high S_{BET} area samples. Therefore, particular attention was given to those parameters that
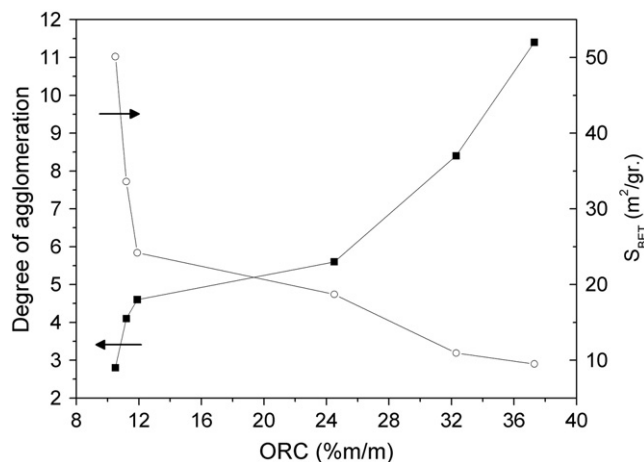

Fig. 11. Degree of agglomeration and S_{BET} as a function of the organic residue content.
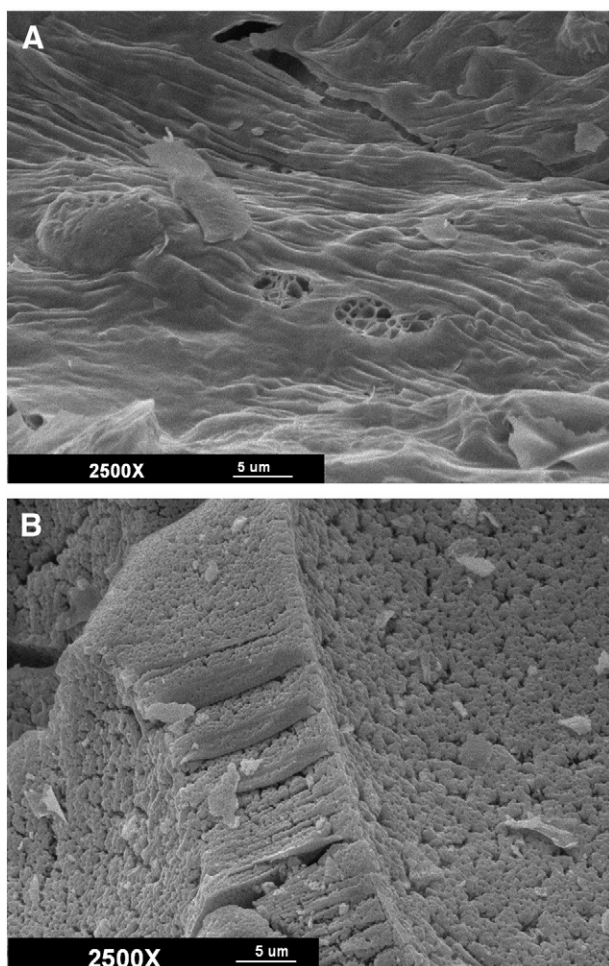
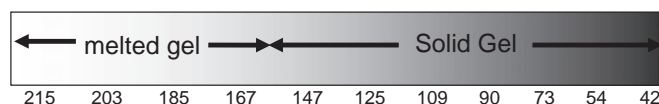**Fig. 12.** A) Z3Y-ala and B) Z3Y-5 ceramic powders. Both at 2500×.

Diagram 2. Temperature distribution (in °C) for the temperature gradient synthesis.

Unfortunately, the content of organic residues had a degrading effect on the S_{BET}. Its increase produced a decrease of the S_{BET} and a consequent increase in the degree of agglomeration. If only the samples with the same Φ (Z3Y-Lys, Z3Y-Ala, Z3Y-Gly, Z3Y-5, Z10Y and Z12Y) are taken into consideration, this tendency is even more pronounced (Fig. 11). This probably occurs because the combustion of the leftover organic residues during the calcination step produces a partial local sintering [11]. As a partial conclusion, then, synthesis routes that produce high combustion temperature and low content of organic residues are ideal in order to produce nanopowders with high S_{BET}.

The influence of the final pH on the crystal structure of the ceramic powder was also studied. For the ZrO_2–2.8 mol% Y_2O_3 samples, a pH value between 2 and 2.5 was necessary to obtain the metastable tetragonal phase. The low combustion temperature of the Z3Y-2 sample, its proximity to the monoclinic/tetragonal limit (ZrO_2–2 mol% Y_2O_3) or maybe an inhomogeneous mixture in the gel due to the low pH, may explain this effect. Nevertheless it will be the focus of a future study. For the 5 mol% Y_2O_3 sample, the crystal structure was independent of final pH (for a pH higher than 0).

Finally, SEM studies were performed to examine the ceramic powders. Similar to what happened in the XAS study, the observed microstructures could be divided into three distinctive groups depending on the fuel: glycine, citric acid and the remaining amino acids. Fig. 12, A and B, shows the microstructure of Z3Y-ala and Z3Y-5, respectively, as a typical example. At low magnification (100×, Fig. S5) both groups appeared similar, showing porous agglomerates of approximately 100 and 250 μm, respectively. When the magnification was increased (2500×, Fig. 12), clear differences were observed. The powders synthesized with citric acid showed several cracks and a more porous surface, while the powders synthesized with amino acid showed few cracks and a smooth surface. The powder synthesized with glycine was an intermediate case, showing a smooth cracked surface with no pores. These microstructures are in accordance with S_{BET} data.

3.4. An additional synthesis route

Putting together all the results presented above, an additional synthesis, Z3Y-H_2O_2, was planned. The citric acid/metal ratio was increased to 5 (to dilute the oxide precursor and generate a low D_{ash}) and 10 ml of 200vol H_2O_2 was added to the precursor solution. H_2O_2 was chosen because it decomposes into H_2O and O_2 and thus it does not leave any solid residue, liberates additional gasses during combustion

generated a high S_{BET} and low degree of agglomeration, also. We can notice an interesting tendency if S_{BET} is arranged in order of increasing combustion temperature: S_{BET} increases with increasing combustion temperature (see Fig. 10). This can be due to the fact that a higher combustion temperature expands the gasses faster and with more violence, thus resulting in smaller aggregates. Subsequently, if more gasses are released, the S_{BET} should increase [1,26]. This is exactly the case of the Z3Y-4/5/6 series: the first sample had a lower S_{BET} (19.2 m²/g) and NH_4NO_3 content (a gas releasing molecule) than the other ones (24.2 and 23.8 m²/g, respectively).

Diagram 1. Flow chart for the combustion synthesis. (gray: stoichiometric route). Ala: alanine. Lys: lysine. Gly: glycine. Cit: citric acid.

Table 2
Structural standards for XAS analysis, see text, and corresponding environments.

Standard	Environment
ZrO_2 monoclinic	7 O with 7 different distances
$ZrSiO_4$	4 O at 2.076 Å
	4 O at 2.294 Å
$ZrOCl_2 \cdot 8H_2O$	3 O with 3 distances about 2.12 Å
	3 O with 3 distances about 2.21 Å
	2 O with 2 distances about 2.32 Å
$BaZrO_3$	6 O at 2.099 Å
Cubic ZrO_2	8 O at 2.226

Table 3
EXAFS analysis results at the Zr K edge for AA precursor gels CN: coordination number. d: Zr – O or Zr – Zr bond length. σ^2: Debye–Waller parameter. ΔEo: energy shift. R: goodness of fit.

Sample	First sphere (Zr – O)			Second sphere (Zr – Zr)			ΔEo (eV)	R (%)
	CN	d (Å)	σ^2 (Å^2)	NC	d (Å)	σ^2 (Å^2)		
Z15Ce	2.3 (5)	2.11 (1)	0.00049 (5)	2.0 (4)	3.53 (2)	0.0051 (5)	2.39	3.60
	3.4 (7)	2.22 (1)						
	1.6 (3)	2.36 (1)						
Z3Y-ala	2.0 (4)	2.12 (1)	0.000051 (5)	2.1 (4)	3.53 (2)	0.0043 (5)	2.69	1.46
	3.4 (7)	2.21 (1)						
	2.0 (4)	2.35 (1)						
Z3Y-Gly-stoi	1.8 (4)	2.11 (1)	0.00031 (3)	3.0 (6)	3.53 (2)	0.0039 (4)	−0.70	1.12
	3.6 (7)	2.20 (1)						
	2.1 (4)	2.32 (1)						
Z3Y-Gly	2.0 (4)	2.12 (1)	0.00019 (2)	2.2 (4)	3.53 (2)	0.0042 (5)	1.12	1.27
	3.5 (7)	2.21 (1)						
	2.0 (4)	2.34 (1)						
Z3Y-Lys-stoi	1.4 (3)	2.10 (1)	0.00049 (5)	3.0 (6)	3.53 (2)	0.0045 (5)	−5.62	1.91
	3.4 (7)	2.20 (1)						
	2.5 (5)	2.32 (1)						
Z3Y-Lys-stoi	2.0 (4)	2.11 (1)	0.00012 (1)	2.7 (5)	3.51 (2)	0.0045 (5)	3.75	3.41
	3.2 (6)	2.22 (1)						
	1.7 (3)	2.35 (1)						

Table 4
EXAFS analysis results at the Zr K edge for Cit precursors gels CN: coordination number. d: Zr – O or Zr – Zr bond length. σ^2: Debye–Waller parameter. ΔEo: energy shift. R: goodness of fit.

Sample	First sphere (Zr – O)			Second sphere				ΔEo (eV)	R (%)
	CN	d (Å)	σ^2 (Å^2)	NC (Zr – Zr)	NC (Zr – C)	d (Å)	σ^2 (Å^2)		
Z3Y-1.25Cit	8 (1)	2.18 (1)	0.0091 (9)	1.6 (3)		3.53 (2)	0.0044 (4)	2.8	2.35
					2.7 (6)	3.52 (2)	0.0047 (5)		
Z3Y-3.75Cit	9 (1)	2.15 (1)	0.0081 (8)	1.4 (13)		3.51 (2)	0.0037 (4)	−1.8	3.45
					4.8 (9)	3.46 (2)	0.0074 (7)		
Z3Y-4	9 (1)	2.15 (1)	0.0080 (8)	1.2 (2)		3.52 (2)	0.0038 (4)	−1.2	2.31
					3.9 (8)	3.49 (2)	0.0047 (5)		
Z3Y-5	9 (1)	2.15 (1)	0.0085 (9)	1.4 (2)		3.51 (2)	0.0036 (4)	−0.2	1.77
					3.8 (8)	3.48 (2)	0.0084 (8)		
Z3Y-6	9 (1)	2.15 (1)	0.0088 (9)	1.3 (2)		3.51 (2)	0.0029 (3)	−2.5	2.69
					4.6 (5)	3.48 (2)	0.0062 (6)		
Z10Y	8 (1)	2.15 (1)	0.0084 (8)	1.6 (3)		3.51 (2)	0.0032 (3)	0	2.26
					4.5 (9)	3.48 (2)	0.0069 (7)		
Z12Y	9 (1)	2.15 (1)	0.0083 (8)	1.6 (3)		3.51 (2)	0.0031 (3)	0.2	2.26
					4.3 (9)	3.48 (2)	0.0065 (7)		

and generates atomic oxygen which helps eliminate the organic residues and elevates the combustion temperature. All these factors were identified to decrease D_{powder} and raise S_{BET}. As predicted, this ceramic powder presented the smallest average crystallite size (8.1 nm), the highest S_{BET} (46.7 m^2/gr, an increase of 80%) and the smaller degree of agglomeration (2.6) of the Z3Y series. Given these excellent results, additional investigation on this new route is currently in progress.

4. Conclusions and final remarks

We presented a detailed study of the effect on the powder morphology of several synthesis parameters of the gel-combustion routes.

Multiple techniques (FTIR, EXAFS) showed that the cations are complexed in the gel and thus maintained in solution ensuring a homogeneous mixture. Homogeneity also demonstrated by the SAXS analysis, reported here for the first time for the whole gelling process. This homogeneity is the origin of the compositional homogeneity of the ceramic powders produced by this synthesis method.

EXAFS analysis also determined that Y was isolated whereas Zr was in its tetramer state, $[Zr_4(OH)_8(16H_2O)]^{8+}$.

It was found that atmospheric oxygen was not necessary for the combustion to occur and that its temperature depended on several factors: nature of the dopant oxide, ceramic composition, type of fuel and fuel/metal ratio, but was practically independent of the synthesis route, final pH (for pH >4) or ammonium content.

Table 5
EXAFS analysis results at the Y K edge for AA and Cit precursor gels. CN: coordination number. d: Zr – O bond length. σ^2: Debye–Waller parameter. ΔEo: energy shift. R: goodness of fit.

Sample	First sphere			ΔEo (eV)	R (%)
	CN	d (Å)	σ^2 (Å^2)		
Z3Y-Gly-stoi	8 (1)	2.39 (1)	0.0063 (6)	2.7	0.92
Z3Y-4	8 (1)	2.35 (1)	0.0084 (8)	1.5	0.87

Table 6

T_{comb} maximum temperature measured during the combustion reaction. % Ox: m/m percentage of the oxide in the gel. D_{ash} and D_{powder}: average crystallite size of the ashes and the ceramic powders, respectively. S_{BET}: BET specific surface area. d: average particle size. d/D_{powder}: degree of agglomeration in the ceramic powder. ORC: organic residue content (% m/m of the ashes).

Gel	T_{comb} (°C) ($\pm$ 15 °C)	% Ox	D_{ash} (nm)	D_{powder} (nm)	S_{BET} (m^2/gr)	d (nm)	d/D_{powder}	ORC
Z3Y-Lys	440	33.7 (1)	[a]	10.9 (5)	11.0 (2)	91 (2)	8.4 (4)	32.3 (1)
Z3Y-Lys-Stoi	440	71.2 (1)	4.0 (5)	10.7 (5)	16.9 (3)	59 (1)	5.4 (3)	11.2 (1)
Z3Y-Ala	518	31.5 (1)	4.0 (5)	9.2 (5)	9.5 (1)	105 (2)	11.4 (5)	37.3 (1)
Z3Y-1.25Cit	540	31.8 (1)	7.2 (5)	9.5 (5)	15.6 (2)	64 (1)	6.8 (4)	26.4 (1)
Z3Y-5	645	18.9 (1)	6.2 (5)	9.0 (5)	24.2 (4)	41.3 (8)	4.6 (2)	11.9 (1)
Z3Y-3.75Cit	600	13.5 (1)	5.1 (5)	10.4 (5)	26.1 (4)	38.3 (8)	3.7 (2)	26.1 (1)
Z3Y-2[b]	250	18.9 (1)	–	–	–	–	–	–
Z3Y-2.5	–	18.9 (1)	6.3 (5)	9.5 (5)	–	–	–	–
Z3Y-4	648	18.9 (1)	6.4 (5)	9.3 (5)	19.2 (3)	52 (1)	5.3 (3)	36.2 (1)
Z3Y-6	642	18.9 (1)	6.2 (5)	10.3 (5)	23.8 (4)	42.0 (8)	4.0 (2)	44.0 (1)
Z3Y-5-SO	[c]	18.9 (1)	6.3 (5)	8.9 (5)	23.9 (4)	41.8 (8)	4.7 (3)	12.0 (1)
Z3Y-H$_2$O$_2$	–	10.5 (1)	5.1 (5)	8.1 (5)	46.7 (7)	21.4 (4)	2.6 (1)	19.5 (1)
Z3Y-Gly	664	24.6 (1)	6.4 (5)	9.6 (5)	18.7 (3)	54 (1)	5.6 (3)	24.5 (1)
Z3Y-Gly-Stoi	653	58.9 (1)	6.3 (5)	9.6 (5)	20.1 (3)	50 (1)	5.1 (3)	8.0 (1)
Z5Y	610	18.9 (1)	6.3 (5)	7.9 (5)	–	–	–	38.5 (1)
Z10Y	739	18.8 (1)	6.4 (5)	7.2 (5)	33.6 (5)	29.8 (6)	4.1 (2)	11.2 (1)
Z12Y	776	18.7 (1)	6.5 (5)	7.0 (5)	50.1 (7)	20.0 (4)	2.8 (1)	10.5 (1)
Z15Ce	1009	19.9 (1)	14.4 (5)	14.4 (5)	–	–	–	4.3 (1)

[a] Amorphous.

[b] 100% monoclinic phase in the ceramic powder.

[c] The temperature could not be measured due to the absorbance of the container.

We identified synthesis conditions to obtain deagglomerated ceramic powders with small average crystallite size and high BET specific surface area.

No comparison can be made with the literature, since one of the main variables identified in this work, the combustion temperature of the solid, is not discussed altogether. A limited number of papers [2,5,11,21,23] calculated it using thermodynamic data assuming an adiabatic approximation. Even fewer reported a measured temperature, but they measured the temperature of the flame [6,10,28] or use a thermocouple [1]. For this reason, we consider that the present paper is an important contribution in order to understand the influence of this important parameter in the morphology of the powders.

Acknowledgments

Appendix A. Supplementary data

Supplementary data to this article can be found online at doi:10.1016/j.powtec.2011.08.013.

References

[1] C.C. Chen, K.T. Huang, J. Mater. Res. 20 (2) (2005) 424–431.
[2] R.D. Purohit, B.P. Sharma, K.T. Pillai, A.K. Tyagi, Mater. Res. Bull. 36 (2001) 2711–2721.
[3] S. Roy, W. Sigmund, F. Aldinger, J. Mater. Res. 14 (4) (1999) 1524–1531.
[4] K.C. Patil, S.T. Aruna, T. Mimani, Curr. Opin. Solid State Mater. Sci. 6 (2002) 507–512.
[5] S.T. Aruna, K.S. Rajam, Mater. Res. Bull. 39 (2004) 157–167.
[6] V. Bedekar, S.V. Chavan, A.K. Tyagi, J. Mater. Res. 22 (3) (2007) 587–594.
[7] W. Zhou, R. Ran, Z.P. Shao, H.X. Gu, W.Q. Jin, N.P. Xu, J. Power Sources 174 (2007) 237–245.
[8] P.K. Patro, A.R. Kulkarni, C.S. Harendranath, Mater. Res. Bull. 38 (2003) 249–259.
[9] F. Li, K. Hu, J. Li, D. Zhang, G. Chen, Nucl. Mater. 300 (2002) 82–90.
[10] S.V. Chavan, A.K. Tyagi, J. Mater. Res. 19 (2004) 3181–3188.
[11] S.R. Nair, R.D. Purohit, A.K. Tyagi, P.K. Sinha, B.P. Sharma, Mater. Res. Bull. 43 (2008) 1573–1582.
[12] I.O. Fábregas, R.O. Fuentes, D.G. Lamas, M.E. Fernández de Rapp, N.E. Walsöe de Reca, M.C.A. Fantini, A.F. Craievich, R.J. Prado, R.P. Millen, M.L.A. Temperini, J. Phys. Condens. Matter 18 (2006) 7863–7881.
[13] I.O. Fábregas, D.G. Lamas, N.E. Walsöe de Reca, M.C.A. Fantini, A.F. Craievich, R.J. Prado, J. Appl. Crystallogr. 41 (2008) 680–689.
[14] A. Pathak, S. Mohapatra, S. Mohapatra, S.K. Biswas, D. Dhak, N.K. Pramanik, A. Tarafdar, P. Pramanik, Am. Ceram. Soc. Bull. 83 (8) (2004) 9301–9306.
[15] J.R. Casanova, I.O. Fábregas, D.G. Lamas, N.E. Walsoe de Reca, G.E. Lascalea, R. Kempf, A.F. Craievich, C.V. Santilli, J. Appl. Crystallogr. 40 (2007) s147–s152.
[16] W.E. Lee, W.M. Rainforth, Ceramic Microstructures: Property Control by Processing, Chapman and Hall, London, 1994 p. 317.
[17] R.E. Juarez, D.G. Lamas, G.E. Lascalea, N.E. Walsöe de Reca, Defects Diffus. Forum 177 (1999) 1–26.
[18] A. Trovarelli, Editor. Catalysis by Ceria and Related Materials, Imperial College Press, London, 2002.
[19] C. Deportes, M. Duclot, P. Fabry, J. Fouletier, A. Hammou, M. Kleitz, E. Siebert, J.L. Souquet, Electrochimie des Solides, Presses Universitaires de Grenoble, Grenoble, 1994.
[20] R. Yaparpalvi, S.K. Loyalka, R.V. Tompson Jr., J. Biomed. Mater. Res. 28 (1994) 1087–1093.
[21] R.K. Lenka, T. Mahata, P.K. Sinha, A.K. Tyagi, J. Alloys Compd. 466 (2008) 326–329.
[22] H.M. Xu, H.G. Yan, Z.H. Chen, Mater. Charact. 59 (2008) 301–305.
[23] Q. Wang, R. Peng, C. Xia, W. Zhu, H. Wang, Ceram. Int. 34 (2008) 1773–1778.
[24] J. Gao, Y. Qi, W. Yang, X. Guo, S. Li, X. Li, Mater. Chem. Phys. 82 (2003) 602–607.
[25] J. Chandradass, M.H. Kim, Bae Dong-Sik, J. Alloys Compd. 470 (2009) L9–L12.
[26] H.C. Shin, K.R. Lee, S. Park, C.H. Jung, S.J. Kim, Jpn. J. Appl. Phys. 35 (1996) L996–L998.
[27] S. Hosseini Vajargah, H.R. Madaah Hosseini, Z.A. Nemati, Mater. Sci. Eng. B 129 (2006) 211–215.
[28] S.T. Mukherjee, V. Bedekar, A. Patra, P.U. Sastry, A.K. Tyagi, J. Alloys Compd. 466 (2008) 493–497.
[29] R. Valiev, Nature 419 (2002) 887–890.
[30] S. Gotthard, Nat. Mater. 3 (2004) 77–85.
[31] A. Thiaville, J. Miltat, Science 284 (1999) 1939–1947.
[32] G. Ozin, A. Arsenault, Nanochemistry: a Chemical Approach to Nanomaterials, Springer, New York, 2005.
[33] D.L. Beke, Z. Erdélyi, I.A. Szabó, C. Cserháti, J. Mestastable Nanocryst. Mater. 19 (2004) 107–111.
[34] P. Heitjans, S. Indris, J. Phys. Condens. Matter 15 (2003) R1257–R1260.
[35] J. Schoonman, Solid State Ionics 157 (2003) 319–335.
[36] A.S. Aricò, P. Bruce, B. Scrosati, J.M. Tarascon, W. van Schalkwijk, Nat. Mater. 4 (2005) 366–372.
[37] J. Maier, Nat. Mater. 4 (2005) 805–809.
[38] M.G. Bellino, D.G. Lamas, N.E. Walsöe de Reca, Adv. Funct. Mater. 16 (2006) 107–111.

[39] A.F. Van Driel, Phys. Rev. Lett. 95 (23) (2005) 236804.
[40] C.A. Leatherdale, W.-K. Woo, F.V. Mikulec, M.G. Bawendi, J. Phys. Chem. B 106 (31) (2002) 7619–7622.
[41] H.C.N. Tolentino, J.C. Cezar, V. Compagnon-Cailhol, E. Tamura, M.C.M. Alves, J. Synchrotron Radiat. 5 (1998) 521–530.
[42] A. Michalowics, F. Champloy, Groupe de Physique des Milieux Denses, Université de Paris XII.
[43] M. Newville, B. Ravel, D. Haskel, J.J. Rehr, E.A. Stern, Y. Yacoby, Phys. B 208–209 (1995) 154–157.
[44] A.L. Ankudinov, B. Ravel, J.J. Rehr, S.D. Conradson, Phys. Rev. B 58 (1998) 7565–7571.
[45] H. Klug, L. Alexander, X-ray Diffraction Procedures for Polycrystalline and Amorphous Materials, John Wiley and Sons, New York, 1974 p. 618.
[46] J. Charles, G. Pouchert, Aldrich Library of FT-IR Spectra, first edition, 1989 United States of America.
[47] R. Nyquist, R. Kagel, IR Spectra of Inorganic Compounds: 3800–45 cm^{-1}, Academic Press, Burlington, 1971.
[48] R.D. Lide, Handbook of Chemistry and Physics, CRC press, Boca raton, 1993–1994.
[49] A. Chatterjee, S.K. Pradhan, A. Datta, M. De, D. Chakravorty, J. Mater. Res. 9 (2) (1994) 263–265.
[50] C. Abraham, J. Mater. Res. 5 (1) (1990) 161–162.
[51] M. Tsubaki, S. Yoshikawa, Biochem. 32 (1) (1993) 164–173.
[52] P.R. Rich, J. Breton, Biochem. 29 (40) (2001) 6441–6449.
[53] P.D. Southon, J.R. Bartlett, J.L. Woolfrey, B. Ben-Nissan, Chem. Mater. 14 (2002) 4313–4319.
[54] F.A. Cotton, G. Wilkinson, Química inorgánica avanzada, Limusa-Noriega, Mexico D.F, 1990, pp. 497–533, (in spanish).
[55] A. Singhal, L.M. Toth, J.S. Lin, K.J. Affholter, J. Am. Chem. Soc. 118 (1996) 11529–11534.
[56] L.M. Toth, J.S. Lin, L.K. Felker, J. Phys. Chem. 95 (1991) 3106–3108.
[57] R. Mouazer, Y. Elmarraki, M. Persin, M. Cretin, J.A. Sarrazin, Colloids Surf., A 216 (2003) 261–273.
[58] T. Kiss, I. SóbáGó, A. Gergely, Pure Appl. Chem. 63 (4) (1991) 597–638.
[59] H.F. Mark, D.F. Othmer, C.G. Overberger, G.T. Seaborg (Eds.), third edition, Kirk-Othmer Encyclopedia of Chemical Technology, vol. 2, Wiley-Interscience, New York, 1978.
[60] A. Mali, A. Ataie, J. Alloys Compd. 399 (2005) 245–250.
[61] F. Zheng, R.K. Bordia, L.R. Pederson, Mater. Res. Bull. 39 (2004) 141–155.
[62] R.S. Guo, Q.T. Wei, H.L. Li, F.H. Wang, Mater. Lett. 60 (2006) 261–265.
[63] A. Mali, A. Ataie, Ceram. Int. 30 (2004) 1979–1983.
[64] R.E. Juárez, D.G. Lamas, G.E. Lascalea, N.E. Walsöe de Reca, J. Eur. Ceram. Soc. 20 (2000) 133–138.
[65] A. Eben, P. Kaupas, Ammonium nitrate production and operational experience, Nitrogen & Methanol 235 (1998) 25–32.
[66] N. Paterson, Y. Zhuo, D. Dugwell, R. Kandiyoti, Energy Fuels 19 (2005) 1016–1022.
[67] S. Goel, Energy Fuels 16 (2002) 823–830.
[68] E.B. Ledesma, Li Chun-Zhu, P.F. Nelson, J.C. Mackie, Energy Fuels 12 (1998) 536–541.
[69] S. Larrondo, M.A. Vidal, B. Irigoyen, A.F. Craievich, D.G. Lamas, I.O. Fábregas, G.E. Lascalea, N.E. Walsöe de Reca, N. Amadeo, Catal. Today 107–108 (2005) 53–59.
[70] G.E. Lascalea, Obtención y propiedades de polvos nanocristalinos y materiales cerámicos de grano submicrométricos basados en zirconia. Tesis de Doctorado en Ciencia y tecnología: Mencion materiales, Universidad Nacional de General San Martin, Buenos Aires, 2004. (in Spanish).
[71] A.S. Monayenkova, S.A. Lezhava, A.A. Popova, L.A. Tiphlova, J. Chem. Thermodyn. 33 (2000) 1679–1686.
[72] S.T. Aruna, K.C. Patil, NanoStruct. Mater. 10 (6) (1998) 955–960.
[73] R.F. Farias, C. Airoldi, J. Inorg. Biochem. 76 (1999) 273–276.
[74] B. Palecz, J. Am. Chem. Soc. 127 (2005) 17768–17771.
[75] B. Palecz, Fluid Phase Equilib. 167 (2000) 253–261.
[76] N.S. Jacobson, Thermodynamic Properties of Some Metal Oxide-Zirconia Systems, National Aeronautics and Space Administration Technical Memorandum 102351, 1989.
[77] T.A. Lee, A. Navrotsky, I. Molodetsky, J. Mater. Res. 18 (4) (2003) 908–918.
[78] A. Navrotsky, P. Simoncic, H. Yokokawa, W. Chen, T. Lee, Faraday Discuss. 134 (2007) 171–180.
[79] T. Shirakami, T. Tojo, T. Atake, T. Mori, H. Yamamura, Thermochim. Acta 267 (1995) 415–420.
[80] T. Shirakami, T. Atake, T. Mori, H. Yamamura, Solid State Ionics 79 (1995) 143–146.
[81] T. Tojo, H. Kawaji, T. Atake, T. Mori, H.J. Yamamura, Chem. Eng. Data 48 (2003) 1479–1482.
[82] C. Degueldre, P. Tissot, H. Lartigue, M. Pouchon, Thermochim. Acta 403 (2003) 267–273.
[83] Y. Moriya, A. Navrotsky, J. Chem. Thermodyn. 38 (2006) 211–223.
[84] G. Adachi, I. Nobuhito, Z.C. Kang, Binary Rare Earth Oxides, Springer, New York, 2004, pp. 814–815.
[85] S.R. Jain, K.C. Adiga, V.R. Pai Verneker, Combust. Flame 40 (1981) 71–79.
[86] M.F. Bianchetti, R.E. Juárez, D.G. Lamas, N.E. Walsöe de Reca, L. Pérez, E. Cabanillas, J. Mater. Res. 17 (2002) 2185–2188.
[87] X. Xin, Z. Lü, Z. Ding, X. Huang, Z. Liu, X. Sha, Y. Zhang, W. Su, J. Alloys Compd. 425 (2006) 69–75.

Dr. Ismael Fábregas studied chemistry at the Universidad de Buenos Aires, Buenos Aires, Argentina. For his PhD, at CINSO (Solid State Research Center), CONICET, Argentina, he carried out research on the crystal structure and local atomic order of zirconia-based nanocrystalline solid solutions. Presently he is a research assistant at CINSO and works in refining of crystal structure, local order and electronic conductivity mainly in materials for solid oxide fuel cells.

Dr. Diego G. Lamas is Associate Professor at the National University of Comahue (Neuquén, Argentina) and Independent Researcher of the National Scientific and Technical Research Council of Argentina. He received his PhD degree in Physics from the University of Buenos Aires, Argentina, in 1999. His investigations are mainly focused on synthesis, characterization, crystallographic and thermodynamic properties and applications of nanostructured materials, mainly nanoceramics for intermediate-temperature solid-oxide fuel cells (IT-SOFCs). During the last decade, he has been the head of the SOFC group at CINSO (Solid State Research Centre), CONICET-CITEFA, Argentina. He is the present vice president of the Argentine Association of Crystallography (AACr).